Wire and arc additive manufacturing of HSLA steel: Effect of Thermal Cycles on Microstructure and Mechanical Properties

Tiago A. Rodrigues [1,]*, V. Duarte [1], Julian A. Avila [2], Telmo G. Santos [1], R. M. Miranda [1], J. P. Oliveira [1]

[1] UNIDEMI, Departamento de Engenharia Mecânica e Industrial, Faculdade de Ciências e Tecnologia, Universidade NOVA de Lisboa, Caparica, Portugal

[2] São Paulo State University (UNESP), Campus of São João da Boa Vista, Av. Profª Isette Corrêa Fontão, 505, Jardim das Flores, 13876-750 - São João da Boa Vista, SP, Brazil

* corresponding author: tma.rodrigues@campus.fct.unl.pt

Abstract

Wire and arc additive manufacturing (WAAM) is a viable technique for the manufacture of large and complex dedicated parts used in structural applications. High-strength low-alloy (HSLA) steels are well-known for their applications in the tool and die industries and as power-plant components. The microstructure and mechanical properties of the as-built parts are investigated, and are correlated with the thermal cycles involved in the process. The heat input is found to affect the cooling rates, interlayer temperatures, and residence times in the 800–500 °C interval when measured using an infrared camera. The microstructural characterization performed by scanning electron microscopy reveals that the microstructural constituents of the sample remain unchanged. i.e., the same microstructural constituents—ferrite, bainite, martensite, and retained austenite are present for all heat inputs. Electron backscattered diffraction analysis shows that no preferential texture has been developed in the samples. Because of the homogeneity in the microstructural features of the as-built parts, the mechanical properties of the as-built parts are found to be nearly isotropic. Mechanical testing of samples shows excellent ductility and high mechanical strength. This is the first study elucidating on the effect of thermal cycles on the microstructure and mechanical properties during WAAM of HSLA steel.

Keywords: Wire and arc additive manufacturing; high-strength low-alloy steels; microstructure characterization; mechanical properties; additive manufacturing.

Graphical Abstract

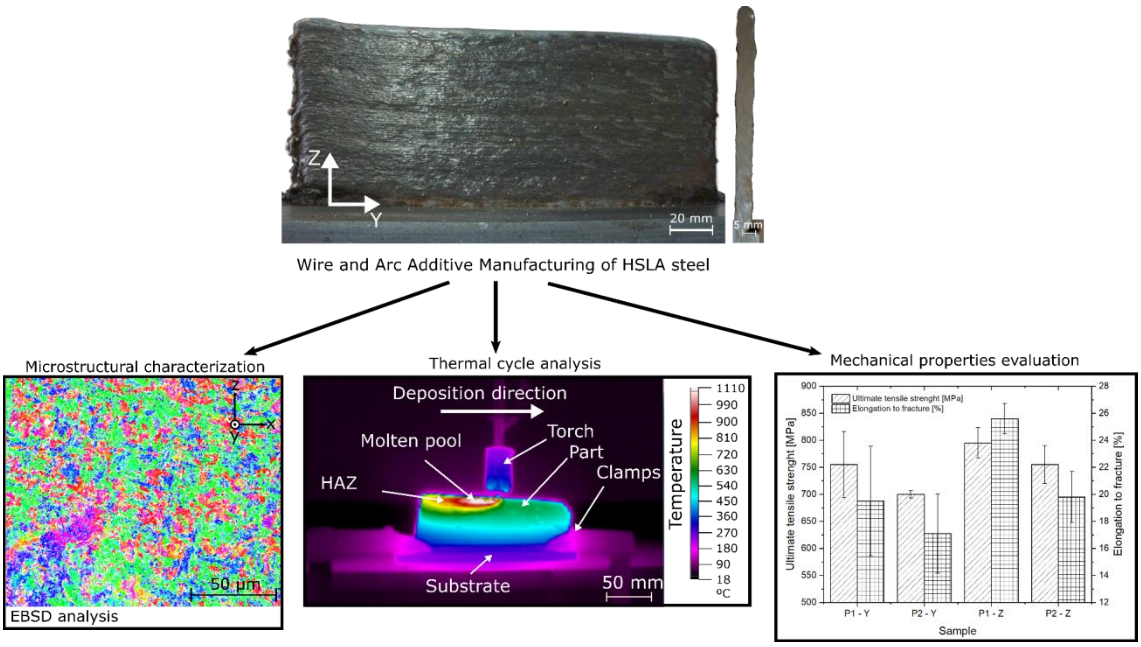

Highlights

- Wire and arc additive manufacturing of HSLA steel was performed.

- Microstructure and mechanical properties were related to the thermal cycles.

- No preferential texture was developed, leading to near-isotropic mechanical properties.

- As-built parts exhibited excellent ductility and high mechanical strength.

1. Introduction

Additive manufacturing (AM) technologies allow the creation of complex parts with tailored mechanical properties within short delivery times [1,2]. In the recent years, AM has gained interest for the design and manufacture of prototypes, with the aerospace, automotive, defense, and medical industries adopting these technologies [3].

Amongst the different AM technologies used for metallic alloys, wire and arc additive manufacturing (WAAM) exhibits several competitive advantages over the laser and electron-beam technologies, such as low capital investment and high deposition rates, and it has also overcome some of the difficulties associated with processing specific alloys [4]. WAAM can be described as a technology combining an electric arc, used as a heat source, and a wire, used as feedstock material, to produce large and complex parts [5]. It uses the fundamental concepts of automatized or robotized processes and arc-welding processes such as gas metal arc welding, gas tungsten arc welding, or plasma arc welding.

Arc-based technologies have been used successfully in AM [5–8]. Even though arc-welding technologies are well known, their use in AM is rather complicated because several phenomena occur simultaneously and a wide range of process parameters must be controlled to fabricate high-quality parts. WAAM is a developing technology, and several challenges remain to be addressed. These include residual stresses and distortions arising from excessive heat input, optimization of process parameters and deposition strategies, poor surface quality of WAAM parts, removal of parts from the substrate, and standardization.

Typically, WAAM uses heat inputs ranging from tens to hundreds of J/mm, and this heat is usually dissipated by conduction through the components and substrates, forced convection through the shielding gas, or radiation to the surrounding environment [9]. However, cooling through conduction becomes difficult as the number of layers increases, as the large area of the substrate causes heat dissipation in the layers deposited first, thereby decreasing the heat accumulation [10]. This heat transfer to the already deposited layers is of major concern, as it affects the cooling rate and thermal cycles of both the previously and currently deposited layers, which can lead to microstructural changes along the part. Therefore, there is a need for process add-ons that allow the control of the thermal cycles acting upon the material. One method of achieving microstructural control is based on the inter-layer temperature, which is defined as the temperature of the previously deposited layer upon the deposition of a new layer [11,12]. The interlayer temperature is considered one of the most important aspects related to the surface waviness and temperature distribution of the parts during fabrication; therefore, it should be selected carefully to avoid undesirable contamination from foreign elements belonging to the previously deposited layers [12,13]. However, process control based on interlayer temperature is difficult, as some of the suitable dwell times may be quite long, reducing the deposition productivity, or very small, urging the use of multiple welding torches, for example. Numerical models have been successfully developed to predict the temperature gradients and their distributions along WAAM walls [14] and, more recently, a model that could accurately predict bead geometry was presented [15].

In the literature, several techniques have been described to regulate the heat dissipation and thermal cycles during WAAM. Mughal et al. [16] investigated the effects of different deposition sequences on the residual stress distribution, stating that layers should be deposited starting from the outside to the center of the part, to reduce potential detrimental effects on the as-built material. Concerning in situ techniques for process control, a finite element analysis of the effect of a coolant hose attached to a welding torch to increase the cooling rate of the underlying beads using air jets was described by Montevecchi et al. [17]. Thermoelectric cooling devices were placed on both sides of the walls being produced, in order to eliminate heat-dissipation differences between the top and bottom layers [18]. A compressed CO_2 jet was used to regulate the interlayer temperature, which was controlled by a pyrometer, to study its effects on bead geometry, surface oxidation, microstructure, and mechanical properties of deposited bead [19]. These types of process developments are beneficial for WAAM, as they can increase the process efficiency and allow the control of microstructure, thereby improving its potential for use in relevant engineering applications.

This work studies the mechanical properties, effects of the heat input on the thermal history, and the subsequent changes induced in the microstructures at various locations in the deposited walls. This investigation also points out the role of the complex thermal history in WAAM, highlighting the importance of controlling the different cooling rates throughout the deposition process.

2. Materials and methods

2.1 Experimental setup

The experimental apparatus consisted of a customized welding torch mounted on a three-axis positioning system, with a working envelope of 2760 × 1960 × 2000 mm (Figure 1). A welding machine from *KEMPY*, with a power source *Pro MIG 3200*, wire feeder, and control unit *Pro MIG 501*, was used to deposit the material over the substrate. The feedstock material was a commercial low-carbon high-strength steel AWS A5.28 ER110S-G wire electrode with a diameter of 1 mm. The chemical composition of the wire is presented in Table 1. The parts were built on mild steel substrates with dimensions of 190 × 100 × 10 mm, which was cleaned and dried prior to the experiment.

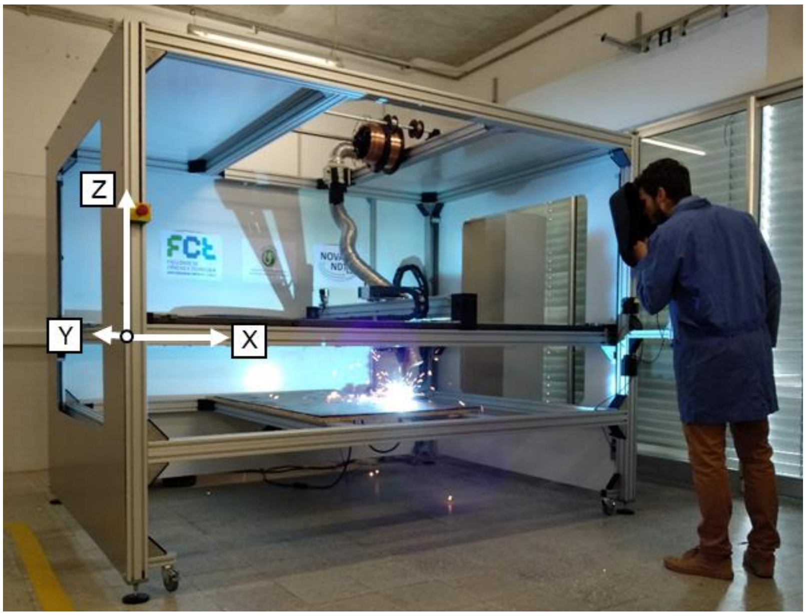

Figure 1 – Working envelope of the wire and arc additive manufacturing (WAAM) machine.

Table 1- Chemical composition of the ER110S-G wire electrode [wt.%].

C	Mn	Si	Ni	Cr	Mo	V	Cu	Fe
0.08	1.70	0.44	1.35	0.23	0.30	0.08	0.25	Balance

The deposition process was instrumented to evaluate the changes in current and voltage during buildup (Figure 2). A short-circuit transfer mode was observed to occur for both depositions studied in this work.

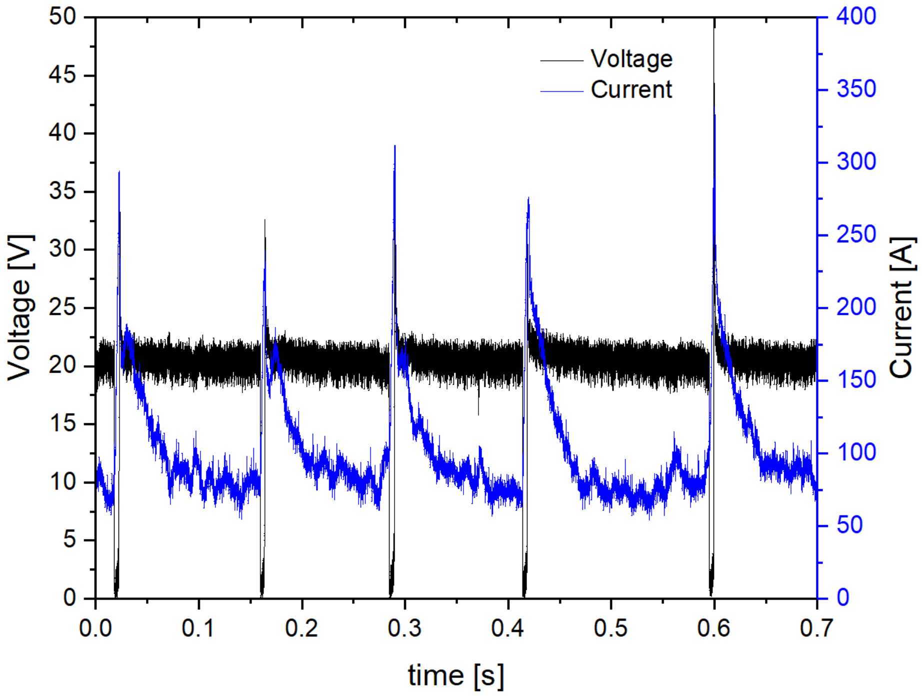

Figure 2 – Voltage and current variations during deposition.

A Fluke TI400 thermographic infrared camera monitored the temperature of the parts during the fabrication; the maximum temperature was limited to 1200 °C. The camera had a measurement accuracy of ±2%, an infrared spectral band up to 14 µm, a refresh rate of 9 Hz, and a resolution of 320 × 240 pixels. The emissivity of an object depends on the temperature, especially, at temperatures as high as that observed in fusion welding. Therefore, an emissivity of 0.84 was used, considering the existing literature [13], which was previously validated with thermocouples. The data were processed using the acquisition software SmartView to measure the temperature at any point during the buildup.

2.2 Sample buildup

The length of the produced walls was set to 170 mm, the contact-tip-to-work distance was 7 mm, and the dwell time between layers was kept constant at one minute. A continuous-wave mode with the electrode connected to the positive terminal (DC+) was used in all experiments. Deposits were made with heat inputs of 511 and 221 J/mm by varying the travel speed from 3.9 to 9 mm/s for samples P1 and P2, respectively. The voltage, current, and wire feed speed were kept constant at 21 V, 95 A, and 3 m/min for both specimens. The shielding gases used were pure Ar (99.999%) and a mixture of Ar + 1% CO_2 + 18% He at a flow rate of 8 and 16 l/min for sample P1 and P2, respectively. The process parameters are summarized in Table 2.

Table 2 - Summary of process parameters.

Sample	Voltage [V]	Current [A]	Wire feed speed [m/min]	Travel speed [mm/s]	Heat input [J/mm]
P1	21	95	3	3.9	511
P2	21	95	3	9	221

According to the deposition strategy, after depositing one layer, the torch ascended a height equal to a bead height and automatically returned to the same starting point. This process was repeated until a height of approximately 100 mm was reached. It is known that an excessive heat sink effect at the beginning of the deposition decreases the weld penetration, resulting in a height increase [20]. However, at the end of the deposition, the increasing difficulty of heat dissipation results in a contrary phenomenon. To overcome this problem, the selected travel speed was lowered by 30% for the first 10 mm and increased by 30% for the last 10 mm, in each deposition. As such, within these regions of the walls, the heat input varied between 730 and 395 J/mm for sample P1 and 315 and 170 J/mm for sample P2, at the beginning and at the end of each deposited layer, respectively. It must be noticed that other deposition strategies can be used in WAAM to compensate the geometrical irregularities as described in [21].

2.3 Characterization techniques

Surface waviness is one of the most important parameters that evaluate the quality of depositions in arc-based AM. As defined in the literature [5], it is the maximum peak-to-valley distance measured from a profile of a given area in the deposited wall. The surface was measured by employing the image treatment software *Adobe Photoshop CS6* and the method described by Geng et al. [22]. For each fabricated sample, five measurements of width, height, and waviness were performed, and the respective average and standard deviation values were determined.

For microstructural characterization, the samples were cut, polished, and etched with Nital (3%). Metallographic analysis was conducted using a *Leica DMI 5000 M* inverted optical microscope. To obtain a deeper insight on the fine microstructural features of the as-built samples, scanning electron microscopy (SEM) coupled with electron backscattered diffraction

(EBSD) was performed. The measurements were performed using a Quanta 650 FEG SEM and a high-speed EBSD system.

Microhardness indentations along the sample's height were made using a *Mitutoyo HM-112 Micro-Vickers Hardness Testing Machine* for a load of 0.5 kg over 10 s, with the distance between indentations being 200 µm. These measurements allowed us to analyze the effects of the thermal cycles on the hardness behavior along the deposited material.

To investigate the evolution of the cooling rate along a wall being deposited, the temperature was monitored at four different tracking points along the height of the wall, at the center of each part as schematically depicted in Figure 3. At these locations, cross sections were removed to pay closer attention to the microstructure and hardness properties.

The mechanical properties were assessed by uniaxial tensile testing and Charpy impact tests, according to ISO 148-1:2016. Thus, two sets of specimens were removed from each produced part, at the zones depicted in Figure 3. The uniaxial tensile and reduced Charpy V notch samples were machined to dimensions of 55 × 8 × 2 mm and 55 × 10 × 2.5 mm, respectively.

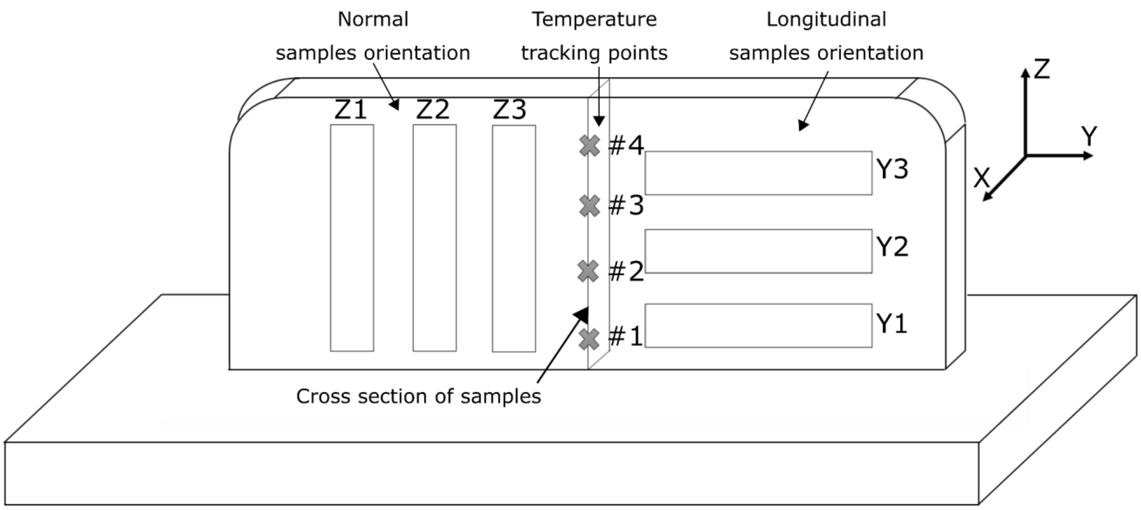

Figure 3 - Schematic representation of the temperature measurement points and location of specimens used for uniaxial tensile and impact testing, and cross section of samples.

3. Results and discussion

3.1 Macroscopic characterization

Figure 4 a) and b) present the overview of the manufactured samples named P1 (high heat input) and P2 (low heat input), respectively. The corresponding transverse cross sections are depicted in Figure 4 c) and d).

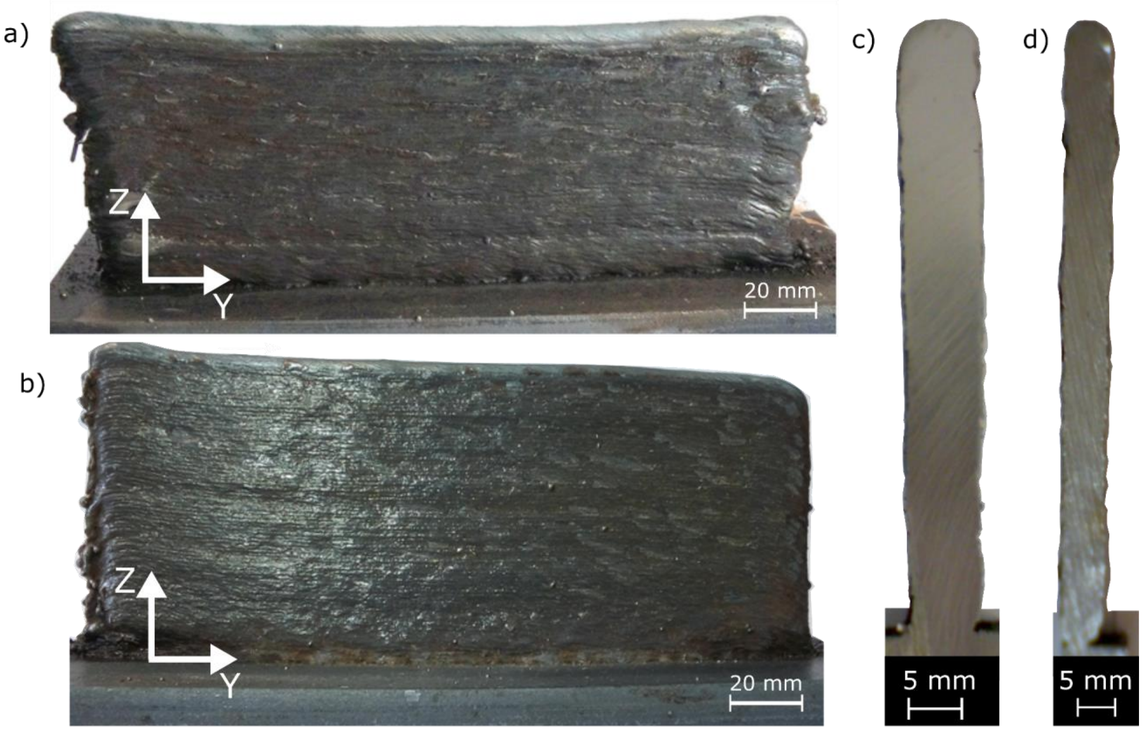

Figure 4 – Aspects of produced parts: a) sample P1 (high heat input); b) sample P2 (low heat input). Corresponding transverse sections: c) sample P1; d) sample P2.

Figure 4 c) and d) depict a narrow bead width in the first layers of each cross section, which is especially evident for sample P2. This occurs because of the rapid cooling to the cold substrate and the small amount of heat accumulated at the beginning of the process. However, with the deposition of the subsequent layers, the substrate temperature increases, which prevents the tightening of the deposited material. Table 3 presents the average and standard deviation results of waviness, width, and height per layer of each sample.

Table 3- Results of the average and standard deviation of waviness, width, and height for each sample.

Sample identification	Heat input [J/mm]	Waviness [μm]	Width [mm]	Height of each layer [mm]
P1	511	356 ± 16	8.8 ± 0.6	1.3 ± 0.1
P2	221	546 ± 66	5.6 ± 0.3	0.9 ± 0.1

Sample P1 was built with a lower travelling speed, resulting in a higher volume of material being deposited per layer. P1 is also the sample with the lowest surface waviness because of the higher interlayer temperature resulting from the heat-dissipation conditions. Its lower waviness is explained by the higher heat input used to deposit the wire feedstock, which increases the interlayer temperature, improving the wettability of the subsequent layers. Additionally, the presence of CO_2 in the shielding gas improves the bead penetration [23]. In order to reduce the surface waviness, a potential approach would require decreasing the interlayer time, which would result in an increase in the interlayer temperature. However, such an approach cannot be viewed from an aesthetic aspect alone, as it can also lead to solid-state transformations that may change the resulting microstructure following a change in the imposed thermal cycles.

As explained previously, the travel speed varies during the deposition of each layer, to compensate for the heat-transfer differences during the building of parts. This is of extreme importance for depositing materials to a similar height in each layer, throughout the process. As shown in Table 4, for sample P1, a difference of approximately 10 mm was measured in the height, between the beginning of the arc striking (78.2 mm) and its extinction (67.3 mm). However, when the heat input was reduced (sample P2), the height difference between the start and finish of a given deposited layer was less than 4 mm, resulting in uniform distribution of material. These results emphasize the critical role of heat input in the control and stability of the molten pool and its solidification: a higher heat input promotes a more significant increase in the temperature of the substrate or the previously deposited layer, which, in turn, hinders heat dissipation, making it more difficult to control the height of the material deposited along a given layer.

Table 4 – Comparison of heights at arc start and end, with travel-speed compensation.

Sample	Height at arc striking [mm]	Height at arc extinguishing [mm]
P1	78.2	67.3
P2	65.4	61.7

While comparing the effects of heat input on the layer waviness and height, it is clear that the effects on part roughness and layer height are contrary. For example, for sample P1, which had a higher heat input, a potential solution to control the differences in the height of each deposited layer could cause an increase in the interlayer time, thus reducing the temperature. However, as discussed before, an increase in the interlayer time results in a rougher surface. Hence, depending on the application and/or subsequent need for post processing (namely machining processes), a trade-off must be made between the roughness and bead height.

3.2 Thermal analysis

In AM, the thermal cycle acting upon the material will significantly influence the microstructure, that is, the solid-state transformations upon cooling and the grain size [24]. Therefore, microstructure-induced changes in the material should be reasoned based on the thermal-cycle analysis of the material. As evidenced before, the thermal cycle acting on the first deposited layers is different from that of the middle or upper layers, because of the heat buildup during production. Figure 5 a) and b) depict the cooling rates due to the subsequent passes above the tracking points for samples P1 and P2, respectively. These cooling rates were measured by calculating the average temperature gradient from 800 to 500 °C ($t_{8/5}$), as it is well-known that, within this temperature range, the cooling rates have a significant impact on the microstructure that can be obtained in the steel [25]. Some of the subsequent passes did not introduce sufficient energy to heat the previous layers to produce temperatures above 500 °C. In those cases, the cooling rates were not calculated.

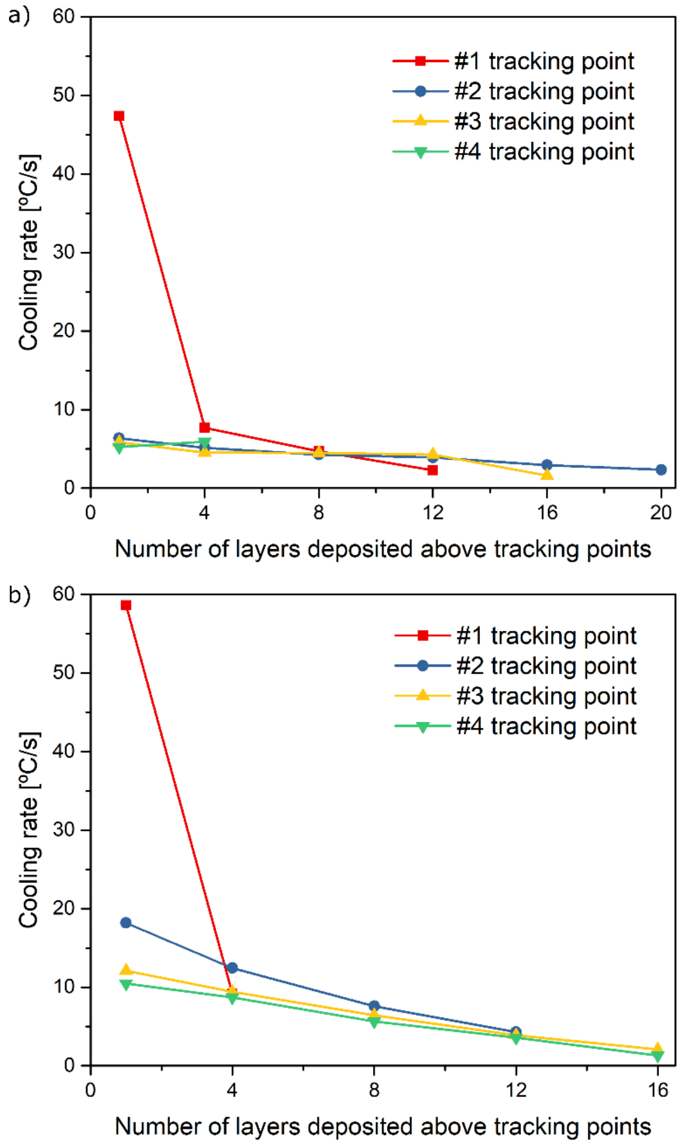

Figure 5 – Cooling rates [°C /s] of samples: a) P1; b) P2.

As expected, the sample fabricated with a higher heat input, P1, experienced lower cooling rates than the sample P2, owing to the higher heat accumulation. Moreover, in both depositions, a large contact area with the substrate facilitated heat dissipation in the first deposited layers, resulting in higher cooling rates. After this point, the cooling rate was dominated by the thermal accumulation caused by the different heat input values used for the deposition: higher heat inputs led to higher amounts of accumulated heat in the already deposited layers, which, in turn, decreased the cooling rate of the material.

Figure 6 depicts the cooling rates (in °C /s) computed for the second tracking point of the analyzed samples, in which the effect of twenty sequential passes is visible. A decrease in the peak temperature and cooling rate is observed with the increase in the distance to the weld pool. On analyzing the peak temperatures after the deposition of each layer, the effect of the heat input was clear: a higher heat input increased the number of times (four in total) a given region surpassed the austenization temperature (approximately 800 °C according to [26]), whereas, for sample P2, this occurred only twice.

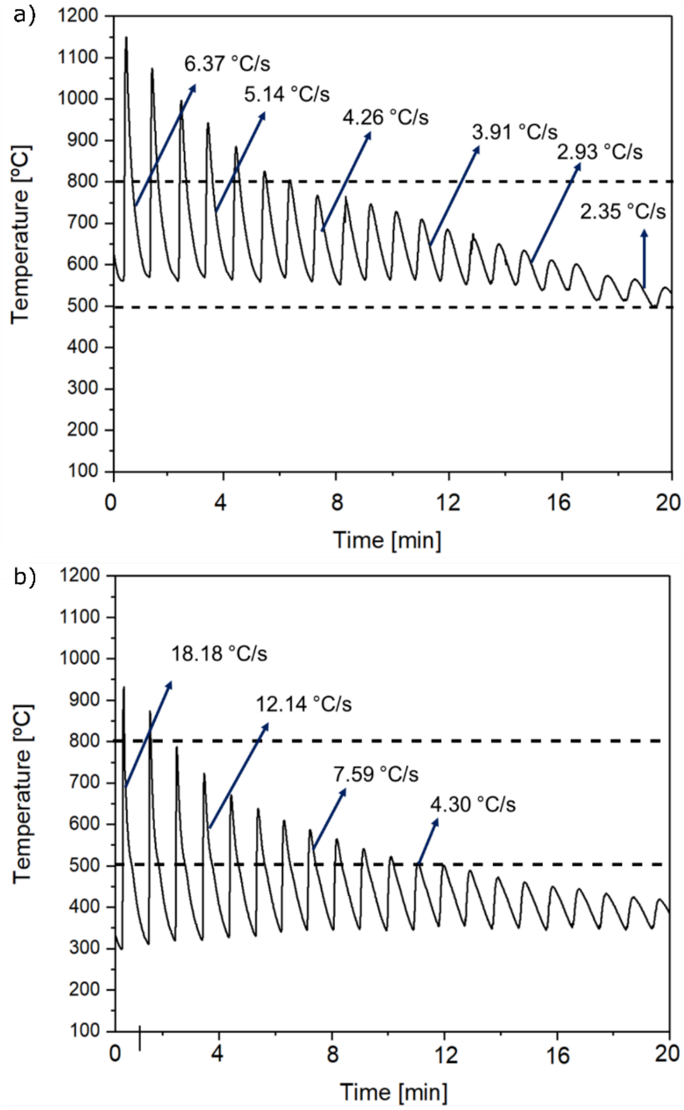

Figure 6 – Sequence of thermal cycles on the second tracking point of samples: a) P1 and b) P2.

During fusion welding of steel, above the Ac_3 temperature where the material is in the austenitic domain, two phenomena can occur: grain growth, at higher temperatures, leading to the formation of the coarse-grain heat-affected zone (HAZ); or recrystallization, forming a fine-grain HAZ. Between Ac_3 and Ac_1, the material is in the biphasic domain of austenite and ferrite; this region is the intercritical zone [27]. Below Ac_1, tempering of the microstructure occurs. From the observed thermal cycles measured between the two tracking points in samples P1 and P2, a change in the microstructure is expected, and this will be discussed when analyzing the microstructural characteristics of the deposited walls.

For steel, the residence time between 800 and 500 °C is known to be critical as it controls the solid-state transformations of the material [28]. For this reason, the residence time of the two tracking points in the 800 to 500 °C interval was determined, and these results are presented in Table 5. However, it must be noted that the residence time count was initiated only when the layer that was being deposited did not induce temperatures above the austenization temperature in the layer where the tracking point was positioned.

Table 5 - Residence time [s] between 800 °C and 500 °C.

Tracking Point	$t_{800-500\,°C}$ [s] for sample:	
	P1	P2
1	947	48
2	1452	362
3	792 (until cooling of last layer)	516
4	90 (until cooling of last layer)	549

It can be observed that higher heat input depositions resulted in longer residence times, with the exception of the fourth tracking point where the subsequently deposited layers always increased the temperature above 800 ◦°C. Thus, in this case, the residence time between 800-500 °C was only initiated when the last layer was deposited. This result demonstrates the importance of controlling the heat and dwell times of each deposition, as well as the proper selection of process parameters, in order to achieve a given desired microstructure.

The interlayer temperature is critical to the deposition strategy in WAAM, as it controls the cooling rate of the deposited layer. Figure 7 depicts the interlayer temperatures measured via thermal camera measurements for both samples.

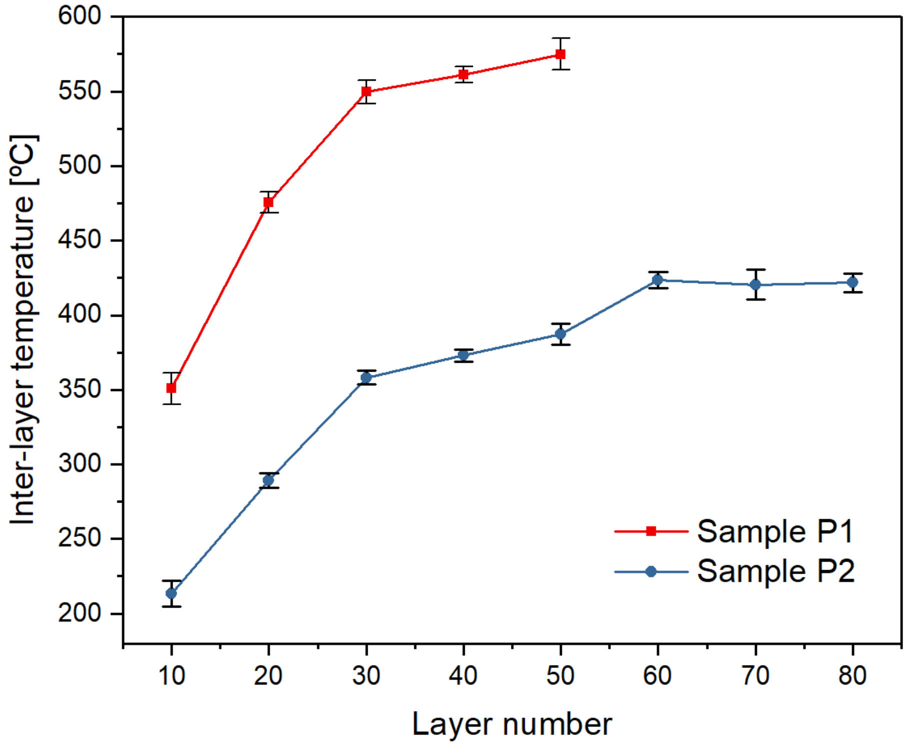

Figure 7 – Variation of interlayer temperature [°C] for P1 and P2 samples.

From the interlayer temperature analysis, it can be observed that the temperature continues to increase, and then stabilizes, presenting evidence of the effect of the substrate temperature on the first-deposited layers. For sample P2, a steady-state condition, that is, with near constant interlayer temperature, was reached approximately at the 60th deposited layer, in contrast to P1 sample that reached a stable interlayer temperature after 30 deposited layers. The interlayer temperature increased faster for sample P1 than for sample P2, because of the heat accumulation effects caused by the higher heat input. To provide the same interlayer temperature for both samples, the dwell time should be increased in sample P1. However, from a management perspective, such adjustments would render increasing lead times.

The thermal field analysis during material deposition can also be used to determine some of the effects of the heat input on the material. Figure 8 depicts a thermographic image of the last-deposited layer for both samples. It can be observed that the width and depth of the HAZ during a single deposition is higher for the higher input sample. Furthermore, the higher heat input clearly increases the temperature in the already-deposited material, and the heat accumulation is noticeable.

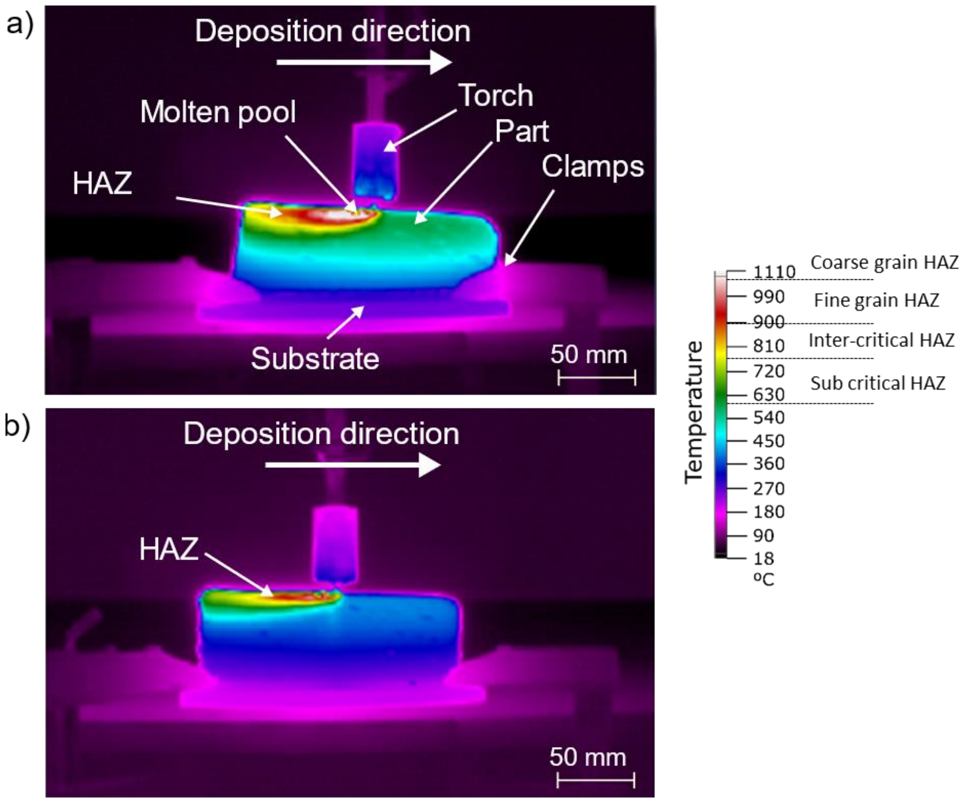

Figure 8 – Thermographic analysis of the last deposited layer for samples: a) P1; b) P2.

3.3 Microscopic observations

Microstructural characterization by means of optical microscopy of the as-built samples, depicted in Figure 9, revealed fully dense parts without cracks, porosity, or lack of fusion. AM techniques where melting occurs have several similarities with fusion-based welding [24]. In the available welding literature, there are multiple procedures such as pre or post-heating, to mitigate cold cracking, which is a very common discontinuity in HSLA steel [29]. However, the deposition of material in a layer-by-a layer process increases the temperature of the previous layers, resulting in a reduction in the cooling rate, thus mitigating the cold-cracking susceptibility. Additionally, the nonexistence of mechanical constraints in WAAM, as it occurs during welding, allows the material to accommodate some of the thermal stresses that are developed during building, which further contributes to reducing the probability of cold cracking.

A more comprehensive view of the microstructure removed from the midsection of both P1 and P2 samples, previously illustrated in Figure 3, is depicted in Figure 9. The grain size is larger in the high heat input sample owing to the heat buildup, which favors grain growth. Additionally, the grain size increases along the height of the produced walls. Ferrite morphologies, acicular and granular morphologies, are observed in Figure 9. Other microconstituents can also be observed; however, their low dimensions hinder their identification by optical microscopy.

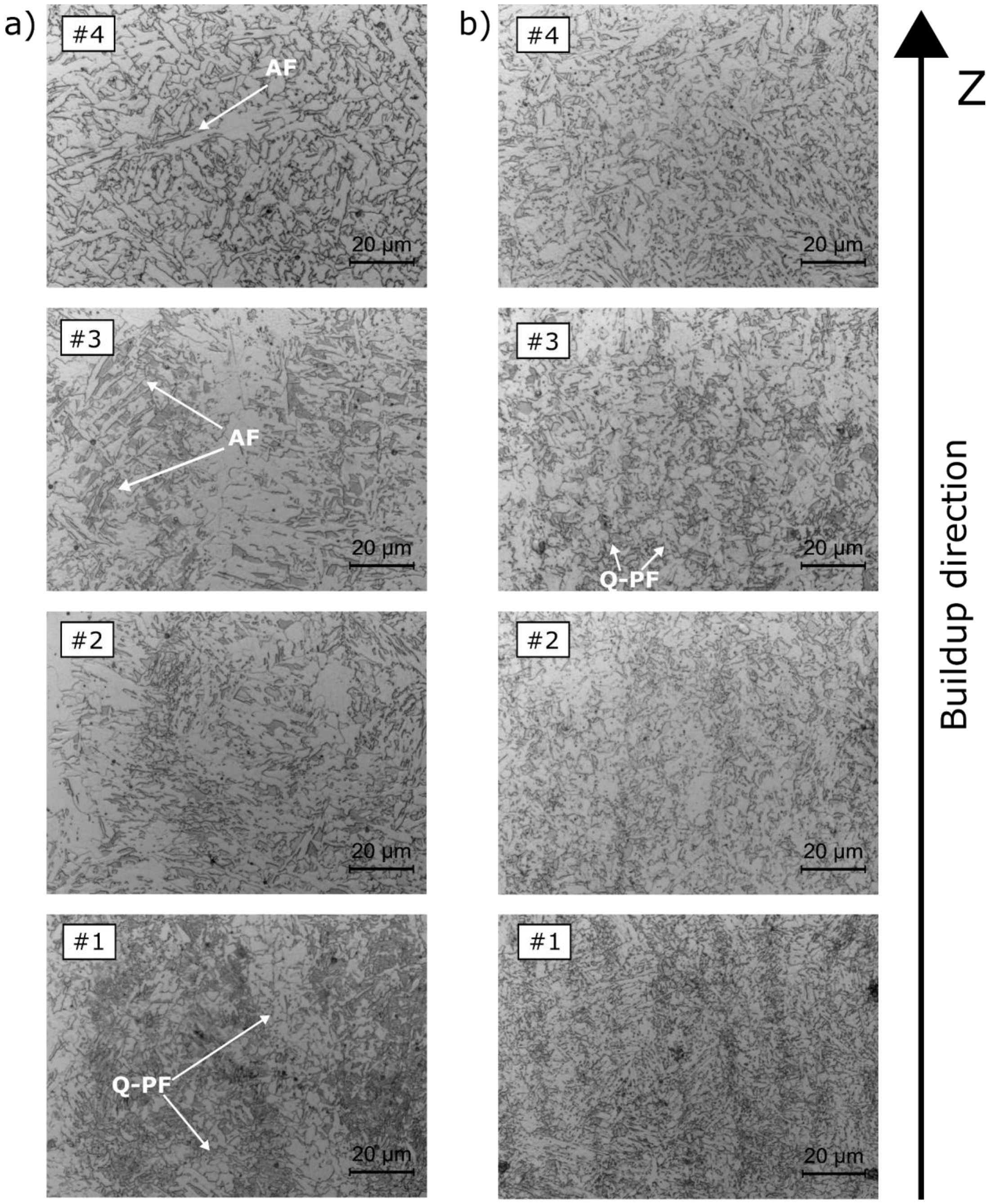

Figure 9 – Cross section micrographs of samples: a) P1 and b) P2 along the height (AF: acicular ferrite; Q-PF: quasi-polygonal ferrite).

The resolution of optical microscopy prevents accurate determination of all the microconstituents that were formed along the built parts. For that reason, SEM aided by EBSD was performed.

Owing to the multiple reheating cycles that any layer experiences (from subsequent depositions), the microstructures of the as-built parts were similar to that of a HAZ in HSLA steel. In such steel, the solid-state transformations can be classified within two temperature regimes: 1300 to 800 °C and 800 to 500 °C. From 1300 to 800 °C, significant austenite grain growth occurs, while in the 800 to 500 °C range, austenite transforms to distinct ferrite morphologies and bainite [26]. Upon cooling from the high-temperature regime, the decomposition from austenite to ferrite occurs, with the formation of allotriomorphic ferrite at the prior austenite grain boundaries. Then, nucleation of the side-plate ferrite may occur at the austenite/ferrite boundaries and extend into the untransformed austenite grains. Acicular ferrite formation is usually associated with oxide inclusions, weld-metal hardenability, and cooling conditions. In the absence of potent inclusions, bainitic ferrite might form upon further cooling [30]. If bainitic ferrite is formed without the presence of carbides, the remaining austenite will be enriched in carbon, which promotes its stability. During the final cooling to room temperature and depending on the carbon content, which influences the M_s and M_f transformation temperatures in carbon steels [31], the remaining austenite may transform fully or partially into martensite. In the latter case, the so-called martensite–austenite (M–A) is formed.

Etching with Nital solution preferentially attacks ferrite. Therefore, other phases such as bainite and M–A constituents are elevated relative to the polygonal ferrite. All these microconstituents are clearly observed in the SEM image of sample P1 in zone #3 within the XY plane in Figure 11 a). Special attention is given to sample P1, as the same microconstituents are observed in sample P2. Figure 11 a) depicts an SEM overview image highlighting the three distinctive microstructures: acicular ferrite (AF), quasi-polygonal ferrite (Q-PF), and bainite. All these phases are predicted by the continuous cooling transformation (CCT) diagram of HSLA steel [32] with a similar chemical composition of the feedstock material used in this work, and are the main constituents of the as-built parts. Fully austenite and martensitic structures could be achieved only at cooling rates higher than 100 °C/s and without reheating cycles, as foreseen by the CCT diagram. Figure 10 depicts the superimposition of some experimental cooling curves on the CCT diagram of the alloy used in this work. It is observed that all reported microstructures are predicted by the CCT diagram, and these depend on the cooling rates experienced by the material. No fully martensitic microstructure was observed in the as-built walls owing to the need to achieve very high cooling rates (> 100 °C/s) which were not obtained during the buildup.

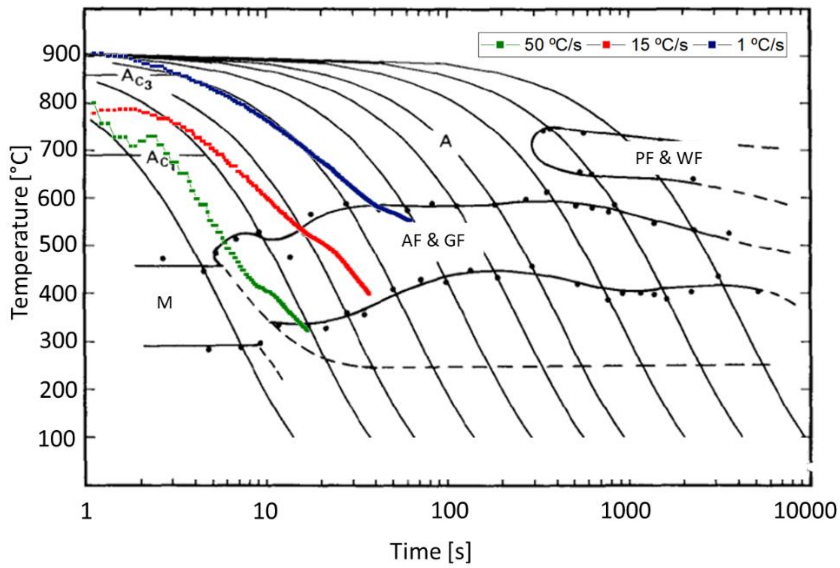

Figure 10 – CCT diagram for the alloy used in this investigation with superimposition of experimental cooling curves (adapted from [32]).

Higher SEM magnifications reveal the presence of M–A (Figure 11 b and c) with a maximum grain size of approximately 10 µm, distributed sparsely along the material. The granular bainite, as shown in Figure 11 c) in a high-contrast image, is represented by a large bainite packet (> 20 µm) enclosed by a red dashed line, with sub grains of sizes less than 1 µm. These sub grains usually present similar crystallographic orientations [33].

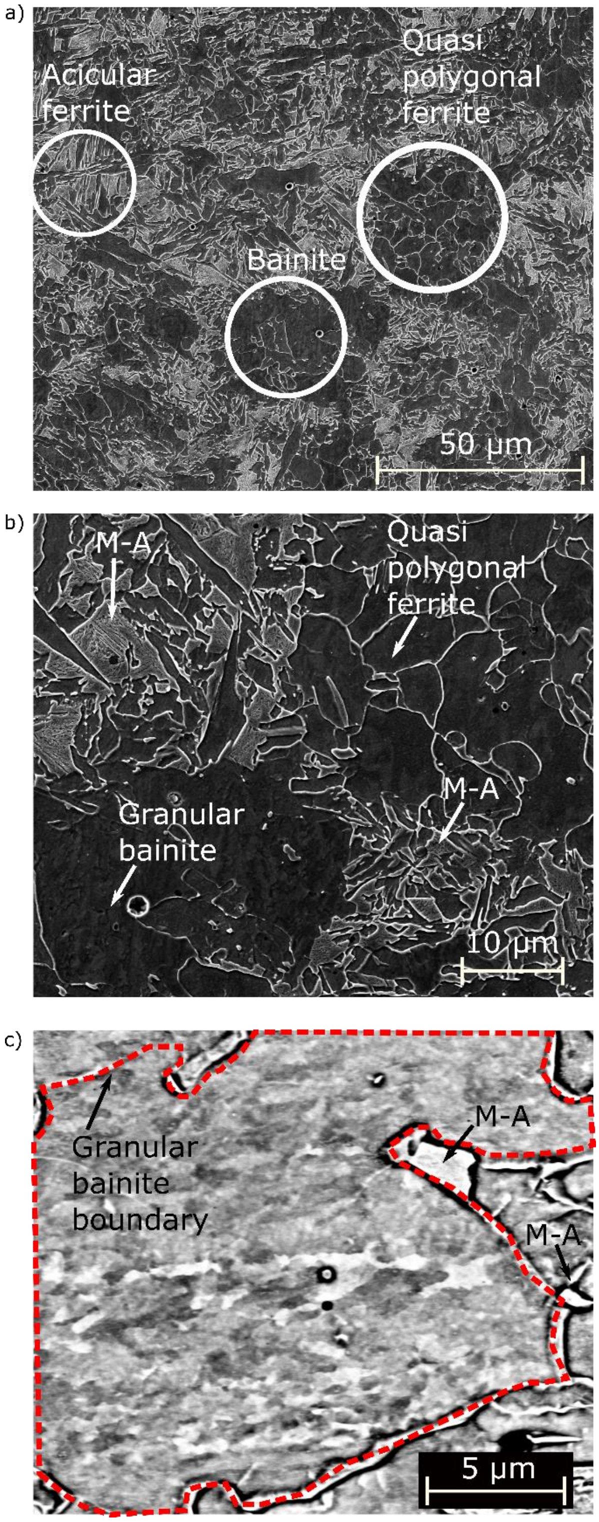

Figure 11 – Scanning electron microscopy (SEM) image of the typical microstructure of the as-built samples (with martensite–austenite (M-A), bainite, acicular ferrite, and quasi-polygonal ferrite): a) overview; b) high-magnification image; c) close-up of a granular bainite packet obtained using a high-contrast detector.

M-A particles are typical microstructures in HSLA steels and are observed for cooling rates between 10 to 40°C/s and stinger-type above these rates [34]. In the case of this research, due to the subsequent heating and cooling of the deposited material it is difficult to track the M-A transformation through the fabrication process, however, mostly blocky-type structures are depicted and these coincide with the morphology reported in the literature [34–36]. The formation of M–A microstructures in low-alloyed steel is attributed to an incomplete transformation from austenite to martensite in the HAZ after reheating to intercritical temperatures [35]. Enrichment of C and Mn have been reported in M-A constituents of a intercritically reheated coarse-grained HAZ (ICCGHAZ) of a HSLA steel [36]. In this work, multipass beads favored the formation of M-A microconstituents, since each following bead caused a reheating at lower temperature and allow elements to stabilized new blocky-type M-A. The presence of necklace-type M–A is in ICCGHAZ is typically undesirable as it can impair fracture toughness [36], nevertheless, no necklace-type M–A were observed in the deposits.

Bainite is formed at intermediate cooling rates, between that of martensite (high cooling rate) and perlite (low cooling rate). The presence of bainitic microstructures usually increases the mechanical strength of the material [37]. Bainite formation is a diffusionless transformation, in which tiny plates known as “sub-units” can be supersaturated in carbon [38]. This leads to carbon partitioning to residual austenite right after the growth of the plates. Such carbon partitioning further complicates the transformation of residual austenite to martensite upon cooling, and favors the formation of M–A regions. The presence of bainite in steel plays a critical role in crack initiation and propagation [35].

To further determine the influence of thermal cycles on the solidification conditions, stability of phases, and developed textures, EBSD measurements were performed. Owing to the large number of steel microstructures, identification of the microconstituents is often problematic [39]. As stated in [39], one of the shortfalls of EBSD, in the quantification of steel microstructures, is the fact that the different morphologies of ferrite have the same crystallographic structure, which may lead to erroneous interpretations. Bainitic microstructures also have lower confidence indexes owing to the large number of dislocations, which is responsible for the high strength and low ductility typical of this phase. EBSD measurements of sample P1 in zone #3, depicted in Figure 12 a), revealed that no significant preferential orientation was developed during the production of the samples. In addition, bainitic areas are often limited by high-angle boundaries, providing another distinct feature to identify such microstructures using EBSD, as shown in Figure 12 b). When the misorientation of these high-angle boundaries is above 40°, the boundaries of the bainite packets can stop the propagation of brittle cracks [33].

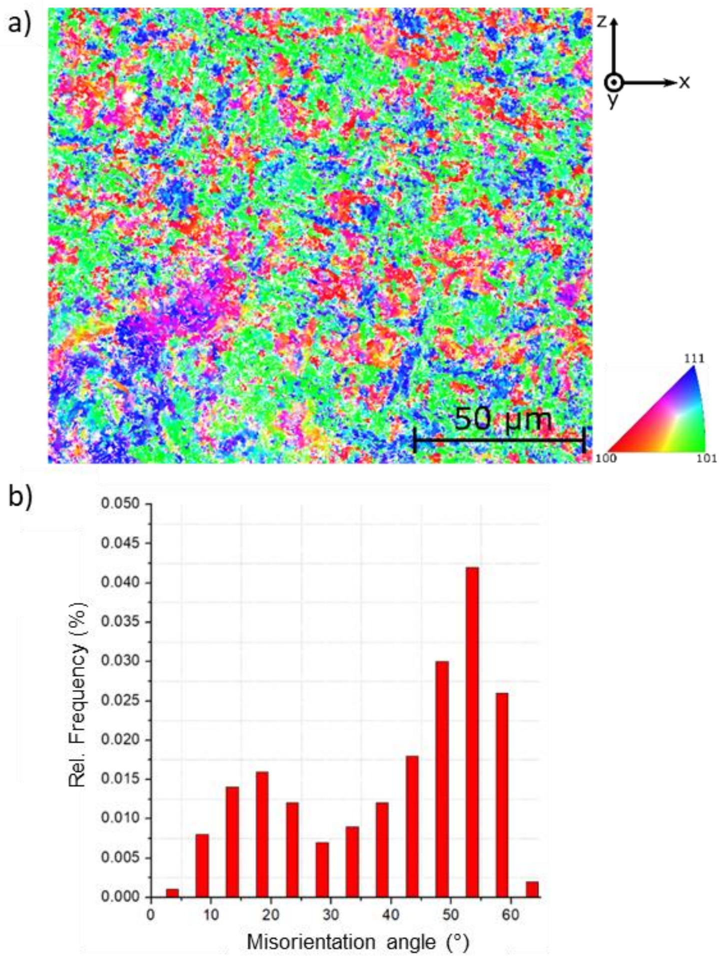

Figure 12 - a) Electron backscattered diffraction (EBSD) inverse pole figure measurements of sample P1; b) misorientation angle.

3.4. Microhardness results

Figure 13 depicts the microhardness distributions near the four tracking points on the cross sections of samples P1 and P2, at a center line along the building height. Globally, for both samples, because of the repeated reheating and thermal accumulation, the grain size was coarser along the height of the sample (building direction), leading to a decrease in hardness. Additionally, the fast cooling rate in the first deposited layers, aided by the cold substrate and its capacity for heat dissipation, justified the higher hardness observed in this region.

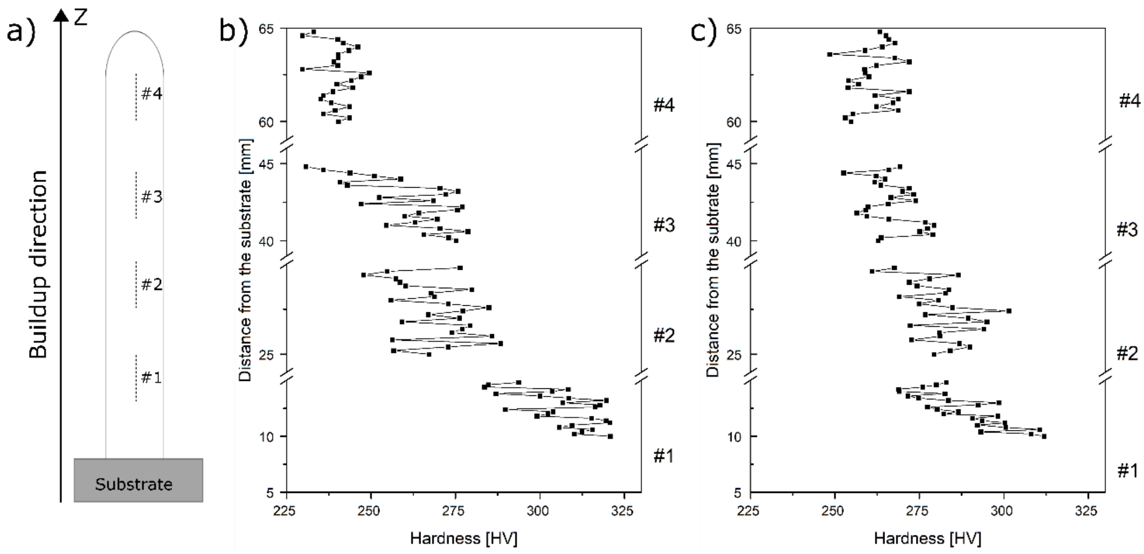

Figure 13 - a) Schematic representation of indentations made on the cross sections of as-built samples. Microhardness profiles along the height of samples: b) P1; c) P2.

In Figure 13, a gradient of hardness is visible along sample P1: in zone #1, the hardness value varies between 283 and 320 HV; in zone #2, between 247 and 288 HV; in zone #3, the hardness value ranges from 230 to 278 HV; and finally, in zone #4, it varies from 229 HV to 250 HV. Sample P2, with a lower heat input during deposition, exhibited slightly lower microhardness along the part height. For sample P2, in zone #1, the hardness changed between 268 and 311 HV, while for zones #2, #3, and #4, it was found to vary within 268 to 300 HV, 256 to 280 HV, and 247 to 277 HV, respectively. It must be noticed that the range of hardness values obtained are in good agreement with those predicted by the CCT diagram for this alloy.

3.5 Uniaxial tensile tests

To evaluate the mechanical properties of the as-built parts, tensile tests were performed along the longitudinal (Y) and normal (Z) directions of the samples obtained (schematically depicted in Figure 3). A summary of the results is presented in Figure 14.

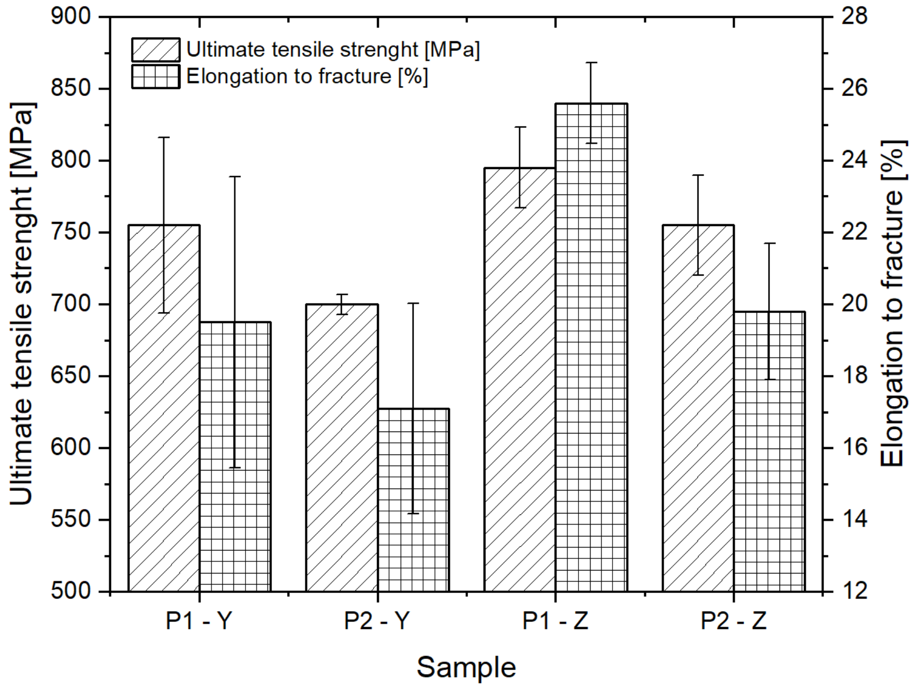

Figure 14 – Ultimate tensile strength (UTS) and elongation to fracture of the tested samples.

Both samples exhibited average values for the ultimate tensile strength (UTS), ranging between 700 and 795 MPa, while the elongation-to-fracture varied from 17.1 to 25.6%. The similar values of UTS obtained along the Y and Z directions for the samples suggested homogeneity of mechanical properties along the height of the parts, regardless of the different cooling rates. Moreover, the elongation-to-fracture values of all samples indicated the good performance of WAAM in the manufacturing of this steel. The existence of ferrite in the microstructure improves the deformation ability of the material, while the formation of bainite leads to an increase in tensile strength. Therefore, the presence of both bainitic and ferritic microstructures produces a material with excellent ductility and mechanical strength.

The SEM analysis of the fracture surfaces revealed a ductile fracture, as evidenced by the massive presence of dimples as depicted in Figure 15 a) and b), corresponding to samples P1 and P2, respectively, when tested along the longitudinal direction. Despite the presence of M–A in the microstructure, no evidence of transgranular cleavage fracture was observed. Therefore, the presence of M–A was not considered detrimental to the mechanical properties of the as-built material, owing to its relatively low volume fraction, which is insufficient to critically change the fracture mode of the as-built parts.

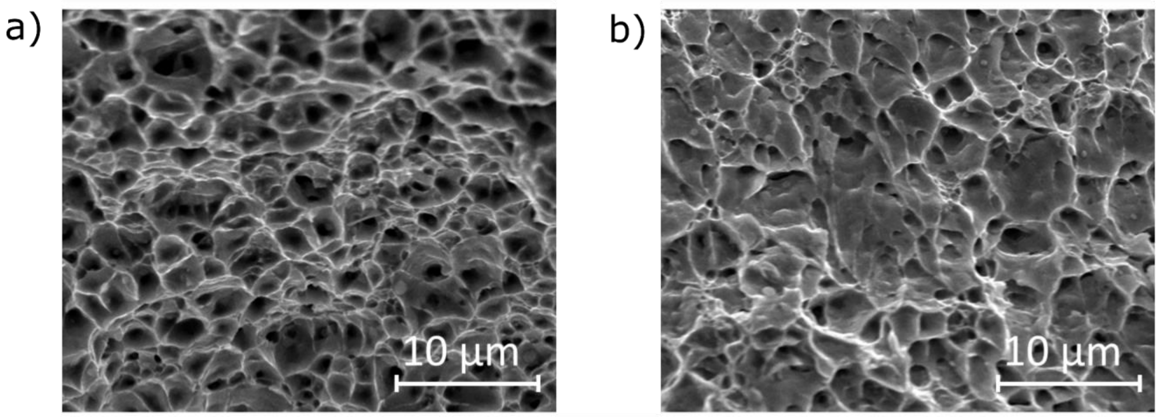

Figure 15 – Scanning electron microscopy (SEM) image of a surface fracture for a sample tested along the longitudinal direction, in specimen: a) P1 and b) P2.

3.6 Charpy impact tests

The impact toughness of the reduced samples extracted along the longitudinal (Y) direction was 15 J, while for those obtained along the normal (Z) direction, the impact toughness increased slightly, to 18 J. In order to convert the acquired data to that of a normalized 10 mm thickness specimen, an empirical hyperbolic-tangent equation [40] was used. The corresponding values were 57 and 71 J, respectively. The impact toughness of the as-received feedstock material was approximately 70 J, according to the wire manufacturer. This difference was within the range of uncertainty of the measurements and the empirical method used, which led to the conclusion that homogeneity of mechanical properties existed between the vertical and horizontal samples, confirming the uniaxial tensile test results.

4. Conclusions

HSLA steel parts were fabricated by WAAM, with different process parameters, and the microstructural evolution along the height of the samples was rationalized based on the complex thermal cycles acting upon the material. The following conclusions were drawn:

- The sample with the highest heat input had less surface waviness, because of the good wettability of the layers over the previously deposited ones.
- As the height increased, the temperature gradient decreased for both depositions (high and low heat input). When a high heat input was used, lower cooling rates were observed and higher residence times occurred in the 800–500 °C temperature range.

- Despite the significantly different heat input values used to build the samples, no significant microstructural changes were observed; the presence of ferrite, bainite, and MA were identified by electron microscopy;
- Owing to the similar microstructures and the fact that no preferential texture was developed, both uniaxial tensile test and Charpy impact test showed similar mechanical properties in the longitudinal (Y) and normal (Z) directions. The as-built parts presented high UTS and excellent ductility.
- Sample P2, with a lower heat input during deposition, exhibited lower and more uniform microhardness along the part height compared to sample P1.

Acknowledgments

TAR, VD, TGS, RMM, and JPO acknowledge Fundação para a Ciência e a Tecnologia (FCT - MCTES) for its financial support via the project UID/EMS/00667/2019. VD acknowledges FCT - MCTES for funding the PhD grant SFRH/BD/139454/2018.

References

[1] U.M. Dilberoglu, B. Gharehpapagh, U. Yaman, M. Dolen, The Role of Additive Manufacturing in the Era of Industry 4.0, Procedia Manuf. 11 (2017) 545–554. doi:10.1016/j.promfg.2017.07.148.

[2] C.R. Cunningham, J.M. Flynn, A. Shokrani, V. Dhokia, S.T. Newman, Invited review article: Strategies and processes for high quality wire arc additive manufacturing, Addit. Manuf. 22 (2018) 672–686. doi:10.1016/j.addma.2018.06.020.

[3] K. V. Wong, A. Hernandez, A Review of Additive Manufacturing, ISRN Mech. Eng. 2012 (2012) 1–10. doi:10.5402/2012/208760.

[4] D. Ding, Z. Pan, D. Cuiuri, H. Li, Wire-feed additive manufacturing of metal components: technologies, developments and future interests, Int. J. Adv. Manuf. Technol. 81 (2015) 465–481. doi:10.1007/s00170-015-7077-3.

[5] P. Kazanas, P. Deherkar, P. Almeida, H. Lockett, S. Williams, Fabrication of geometrical features using wire and arc additive manufacture, Proc. Inst. Mech. Eng. Part B J. Eng. Manuf. 226 (2012) 1042–1051. doi:10.1177/0954405412437126.

[6] A. Addison, J. Ding, F. Martina, H. Lockett, S. Williams, X. Zhang, Manufacture of

Complex Titanium Parts using Wire+Arc Additive Manufacture, Titan. Eur. 2015 Conf. (2015) 14.

[7] J. Ding, P. Colegrove, F. Martina, S. Williams, R. Wiktorowicz, M.R. Palt, Development of a laminar flow local shielding device for wire + arc additive manufacture, J. Mater. Process. Technol. 226 (2015) 99–105. doi:10.1016/j.jmatprotec.2015.07.005.

[8] S.W. Williams, F. Martina, A.C. Addison, J. Ding, G. Pardal, P. Colegrove, Wire + Arc Additive Manufacturing, Mater. Sci. Technol. 32 (2016) 641–647. doi:10.1179/1743284715Y.0000000073.

[9] B.E. Carroll, T.A. Palmer, A.M. Beese, Anisotropic tensile behavior of Ti-6Al-4V components fabricated with directed energy deposition additive manufacturing, Acta Mater. 87 (2015) 309–320. doi:10.1016/j.actamat.2014.12.054.

[10] H. Zhao, G. Zhang, Z. Yin, L. Wu, A 3D dynamic analysis of thermal behavior during single-pass multi-layer weld-based rapid prototyping, J. Mater. Process. Technol. 211 (2011) 488–495. doi:10.1016/j.jmatprotec.2010.11.002.

[11] Y. Ma, D. Cuiuri, C. Shen, H. Li, Z. Pan, Effect of interpass temperature on in-situ alloying and additive manufacturing of titanium aluminides using gas tungsten arc welding, Addit. Manuf. 8 (2015) 71–77. doi:10.1016/j.addma.2015.08.001.

[12] H. Geng, J. Li, J. Xiong, X. Lin, Optimisation of interpass temperature and heat input for wire and arc additive manufacturing 5A06 aluminium alloy, Sci. Technol. Weld. Join. 22 (2017) 472–483. doi:10.1080/13621718.2016.1259031.

[13] D. Yang, G. Wang, G. Zhang, Thermal analysis for single-pass multi-layer GMAW based additive manufacturing using infrared thermography, J. Mater. Process. Technol. 244 (2017) 215–224. doi:10.1016/j.jmatprotec.2017.01.024.

[14] J. Xiong, R. Li, Y. Lei, H. Chen, Heat propagation of circular thin-walled parts fabricated in additive manufacturing using gas metal arc welding, J. Mater. Process. Technol. 251 (2018) 12–19. doi:10.1016/j.jmatprotec.2017.08.007.

[15] W. Ou, T. Mukherjee, G.L. Knapp, Y. Wei, T. Debroy, International Journal of Heat and Mass Transfer Fusion zone geometries , cooling rates and solidification parameters during wire arc additive manufacturing, 127 (2018) 1084–1094.

doi:10.1016/j.ijheatmasstransfer.2018.08.111.

[16] M.P. Mughal, H. Fawad, R.A. Mufti, M. Siddique, Deformation modelling in layered manufacturing of metallic parts using gas metal arc welding: Effect of process parameters, Model. Simul. Mater. Sci. Eng. 13 (2005) 1187–1204. doi:10.1088/0965-0393/13/7/013.

[17] F. Montevecchi, G. Venturini, N. Grossi, A. Scippa, G. Campatelli, Heat accumulation prevention in Wire-Arc-Additive-Manufacturing using air jet impingement, Manuf. Lett. 17 (2018) 14–18. doi:10.1016/j.mfglet.2018.06.004.

[18] F. Li, S. Chen, J. Shi, Y. Zhao, H. Tian, F. Li, S. Chen, J. Shi, Y. Zhao, H. Tian, Thermoelectric Cooling-Aided Bead Geometry Regulation in Wire and Arc-Based Additive Manufacturing of Thin-Walled Structures, Appl. Sci. 8 (2018) 207. doi:10.3390/app8020207.

[19] B. Wu, Z. Pan, D. Ding, D. Cuiuri, H. Li, Z. Fei, The effects of forced interpass cooling on the material properties of wire arc additively manufactured Ti6Al4V alloy, J. Mater. Process. Tech. (2018). doi:10.1016/j.jmatprotec.2018.03.024.

[20] Y.M. Zhang, Y. Chen, P. Li, A.T. Male, Weld deposition-based rapid prototyping: A preliminary study, J. Mater. Process. Technol. 135 (2003) 347–357. doi:10.1016/S0924-0136(02)00867-1.

[21] J. Xiong, Z. Yin, W. Zhang, Forming appearance control of arc striking and extinguishing area in multi-layer single-pass GMAW-based additive manufacturing, Int. J. Adv. Manuf. Technol. 87 (2016) 579–586. doi:10.1007/s00170-016-8543-2.

[22] F.Z. Haibin Geng, Jinglong Li, Jiangtao Xiong, Xin Lin, Dan Huang, Formation and improvement of surface waviness for additive manufacturing 5A06 aluminium alloy component with GTAW system, Rapid Prototyp. Journa. (2018). doi:10.1108/JOCM-07-2016-0124.

[23] C.L. Jenney, A. O’Brien, Welding handbook-II part I, 1991.

[24] J.P. Oliveira, A.J. Cavaleiro, N. Schell, A. Stark, R.M. Miranda, J.L. Ocana, F.M. Braz Fernandes, Effects of laser processing on the transformation characteristics of NiTi: A contribute to additive manufacturing, Scr. Mater. 152 (2018) 122–126.

doi:10.1016/j.scriptamat.2018.04.024.

[25] V.N. Lazić, A.S. Sedmak, M.M. Živković, S.M. Aleksandrović, R.D. Čukić, R.D. Jovičić, I.B. Ivanović, Theoretical-experimental determining of cooling time (t8/5) in hard facing of steels for forging dies, Therm. Sci. 14 (2010) 235–246. doi:10.2298/TSCI1001235L.

[26] Y. Shi, Z. Han, Effect of weld thermal cycle on microstructure and fracture toughness of simulated heat-affected zone for a 800 MPa grade high strength low alloy steel, J. Mater. Process. Technol. 207 (2008) 30–39. doi:10.1016/j.jmatprotec.2007.12.049.

[27] C.L. Davis, J.E. King, Effect of cooling rate on intercritically reheated microstructure and toughness in high strength low alloy steel, Mater. Sci. Technol. 9 (1993) 8–15. doi:10.1179/026708393790171494.

[28] T. DebRoy, H.L.L. Wei, J.S.S. Zuback, T. Mukherjee, J.W.W. Elmer, J.O.O. Milewski, A.M.M. Beese, A. Wilson-Heid, A. De, W. Zhang, Additive manufacturing of metallic components – Process, structure and properties, Prog. Mater. Sci. 92 (2018) 112–224. doi:10.1016/j.pmatsci.2017.10.001.

[29] V.S.R. Murti, P.D. Srinivas, G.H.D. Banadeki, K.S. Raju, Effect of heat input on the metallurgical properties of HSLA steel in multi-pass MIG welding, J. Mater. Process. Tech. 37 (1993) 723–729. doi:10.1016/0924-0136(93)90131-O.

[30] S.S. Babu, The mechanism of acicular ferrite in weld deposits, 8 (2004) 267–278. doi:10.1016/j.cossms.2004.10.001.

[31] C. Capdevila, F.G. Caballero, C.G. de Andrés, Determination of Ms Temperature in Steels: A Bayesian Neural Network Model., ISIJ Int. 42 (2002) 894–902. doi:10.2355/isijinternational.42.894.

[32] S.W. Thompson, D.J. Vin Col, G. Krauss, Continuous cooling transformations and microstructures in a low-carbon, high-strength low-alloy plate steel, Metall. Trans. A. 21 (1990) 1493–1507. doi:10.1007/BF02672564.

[33] J.A. Avila, J. Rodriguez, P.R. Mei, A.J. Ramirez, Microstructure and fracture toughness of multipass friction stir welded joints of API-5L-X80 steel plates, Mater. Sci. Eng. A. 673 (2016) 257–265. doi:10.1016/j.msea.2016.07.045.

[34] J. Avila, J.D. Escobar, B. Cunha, W. Magalhães, P. Mei, J. Rodriguez, H. Pinto, A. Ramirez,

Physical simulation as a tool to understand friction stir processed X80 pipeline steel plate complex microstructures, J. Mater. Res. Technol. 01 (2018) 1–10. doi:10.1016/j.jmrt.2018.09.009.

[35] A. Lambert-Perlade, A.F. Gourgues, J. Besson, T. Sturel, A. Pineau, Mechanisms and modeling of cleavage fracture in simulated heat-affected zone microstructures of a high-strength low alloy steel, Metall. Mater. Trans. A Phys. Metall. Mater. Sci. 35 (2004) 1039–1053. doi:10.1007/s11661-004-1007-6.

[36] X. Li, C. Shang, X. Ma, B. Gault, S.V. V. Subramanian, J. Sun, R.D.K.D.K. Misra, Elemental distribution in the martensite–austenite constituent in intercritically reheated coarse-grained heat-affected zone of a high-strength pipeline steel, Scr. Mater. 139 (2017) 67–70. doi:10.1016/j.scriptamat.2017.06.017.

[37] S. Kang, J.G. Speer, R.W. Regier, H. Nako, S.C. Kennett, K.O. Findley, The analysis of bainitic ferrite microstructure in microalloyed plate steels through quantitative characterization of intervariant boundaries, Mater. Sci. Eng. A. 669 (2016) 459–468. doi:10.1016/j.msea.2016.05.111.

[38] F.G. Caballero, H.K.D.H. Bhadeshia, Very strong bainite, Curr. Opin. Solid State Mater. Sci. 8 (2004) 251–257. doi:10.1016/j.cossms.2004.09.005.

[39] S.L. Shrestha, A.J. Breen, P. Trimby, G. Proust, S.P. Ringer, J.M. Cairney, An automated method of quantifying ferrite microstructures using electron backscatter diffraction (EBSD) data, Ultramicroscopy. 137 (2014) 40–47. doi:10.1016/j.ultramic.2013.11.003.

[40] K. Wallin, Upper shelf energy normalisation for sub-sized charpy- V specimens, Int. J. Press. Vessel. Pip. 78 (2001) 463–470. doi:10.1016/S0308-0161(01)00063-1.